J. R. Castrejon-Pita, E. Betton, K. J. Kubiak, M. C. T. Wilson, and I. M. Hutchings. The dynamics of the impact and coalescence of droplets on a solid surface, Biomicrofluidics, 5 014112 (2011).

The dynamics of the impact and coalescence of droplets

J. R. Castrejón-Pita, E. Betton, K. J. Kubiak[§], M. C. T. Wilson[§], and I. M. Hutchings

Institute for Manufacturing, University of Cambridge,
17 Charles Babbage Road, Cambridge, CB3 0FS, United Kingdom. and
[§]*School of Mechanical Engineering, University of Leeds, Leeds, LS2 9JT, United Kingdom*

A simple experimental setup used to study the impact and coalescence of deposited droplets is presented. Droplet impact and coalescence are investigated by high speed particle image velocimetry. Experimental velocity fields near the liquid-substrate interface are presented for the impact and coalescence of 2.4 mm size droplets of glycerine and water impacting on a flat transparent substrate in air. The experimental arrangement images the droplet inner flow from below the substrate by a high speed camera and continuous laser light. Experimental results are in the form of digital images that are processed by particle image velocimetry and image processing algorithms to obtain velocity fields, droplet properties and contact lines. Experimental results are also compared with numerical simulations by lattice Boltzmann method. Numerical and experimental results confirm that the coalescence of impacting droplets improve mixing at the relaxation stage.

Keywords: Droplets, Velocimetry, Coalescence, Lattice Boltzmann.

I. INTRODUCTION

The study of the impact and coalescence of droplets is of prime importance to the inkjet industry as it is the ultimate factor determining the quality of printing. In addition, the coalescence of droplets is a mechanism with potential applications for the mixing of reagents in microfluidic systems, biological materials and the printing of electronics, [1–3]. Coalescence occurs throughout nature and industry, from rain drop formation to rapid prototyping and sintering. With the inkjet industry expanding into new areas of manufacturing, the accuracy of drop deposition is becoming paramount. For applications such as printed circuit boards or depositing biological materials, the final drop shape and position are essential to the functionality of the final product. Similarly for microfluidics where two substances require mixing, the rate and extent of mixing must be known for chemical reactions to be controlled. In order to rely on drop coalescence for these applications it is essential to understand both the internal and the free surface dynamics.

Several investigations have been carried out to study the dynamics of two sessile drops coalescing. In these experiments, the first drop is placed on a substrate and a second drop is formed next to it by pumping fluid through the substrate until the second drop contacts the first and coalescence takes place, [1] and [4]. This method is treated as having two sessile drops as the second drop is usually expanded very slowly. In these experiments, the rapid neck growth at the point of connection between the two drops is observed from above [5] or/and the side [4]. So far, these studies have shown that the expansion of the neck is driven by surface tension and is opposed by inertial or viscous forces. In particular, it has been demonstrated that the diameter of the meniscus between the two coalescing drops grows in time following a power law. This behavior has been found in the coalescence of mercury droplets, in the coalescence of thin viscous drops spreading due to surface tension and in the early stages of spreading of both viscous and inviscid fluids, [5–8]. These investigations focus their attention on externally measured properties such as contact angles, composite diameters and droplet radii, and not on studying the inner dynamics of the droplet flows.

Many previous experimental works have been performed to visualize the internal motion of droplets. The visualization of the internal flow of a single drop deposited on a surface has demonstrated the existence of symmetric circulation flows which either ascend or descend at the axis of symmetry depending on the motion of the contact line, [3]. Additionally, experiments of two differently coloured droplets coalescing have identified the time scales in which the mixing of fluid occurs, [1]. Quantitative measurement techniques, such as Particle Image Velocimetry (PIV), on sessile or coalescing droplets encounter several limitations, the most important being the optical distortion effects produced by the differences of refractive indexes between the droplet fluid, the substrate material and the medium in which the fluid is jetted (commonly air), [9]. Experiments within index-matched liquids have been conducted using dual-filed and tomographic PIV. These experiments have given an accurate insight into the internal flow of coalescing drops, rebound properties and therefore the mixing behaviour, [10] and [11]. Apart from these investigations, little quantitative experimental work on the internal flow of drops during impact and coalescence in air has been carried out.

Drop coalescence occurring between two static drops can be divided into three stages. During the initial stage the drop edges meet and coalescence occurs. This begins with the formation of a thin liquid bridge between the two drops, which then increases in width with a temporal power law, [1]. During this stage the contact line does not move. After this the neck relaxes in the inter-

mediate stage. The contact line of the drop begins to move and the curvature of the drop surface changes from concave to convex in order to minimize surface energy. The final stage occurs as the drop relaxes into a spherical drop. There is minimal movement of the contact line during this phase as the drop forms a spherical cap. This is driven by surface tension forces in order to reach equilibrium.

This work presents a novel approach for the application of particle image velocimetry on the impact and coalescence of two non-sessile droplets. The experimental setup is simple and can be applied to non-matching refractive index systems. Briefly, these experiments consists of impacting droplets on a rectangular transparent substrate to observe the internal dynamics through and from below the substrate. In this way, the differences of refractive index do not distort the view, no reconstruction algorithms are required and a clear visualization can be done in a two phase system (air/liquid). In addition, this paper combines shadowgraph imaging on a side-view plane and a digital image analysis to extract the traditional geometric properties of the coalescence phenomenon such as dynamic contact angles, composite diameters and neck height and width. Droplets of 2.4 mm diameter with Newtonian properties are used in these experiments. Experimental results are compared with numerical simulations based on the lattice Boltzmann method.

A. Experimental setup

A diagram of the experimental setup is shown in Fig. 1. As mentioned previously, the aim of these experiments is to study the internal flow and the dynamics of droplets during deposition and coalescence. The experiments consist of depositing a droplet adjacent to a sessile droplet resting on a transparent substrate. Two imaging arrangements were used for these aims: an experimental setup visualizing the inner droplet dynamics from behind the substrate and a shadowgraph system to observe the impact and coalescence behavior from a side view.

In all experiments, the position, size and speed of the droplets and the impact properties are controlled by a large scale printhead which has been described elsewhere, [14]. This printhead consists of a closed liquid reservoir containing a flexible membrane on one side and a nozzle orifice opposite to it. The membrane transmits the motion produced by a mechanical actuator to produce the pressure wave required to jet the droplet. The printhead is operated in a drop on demand mode where the speed and size of the produced droplets are adjusted by the waveform sent to the printhead actuator (a V201 LDS vibrator). For these experiments, a 2.2 mm nozzle was used on the printhead with a solution of 85% glycerine on water to produce Newtonian droplets. Single pressure pulses were used on the actuator and adjusted to produce the desired speed and size of the droplets. The measured properties of these droplets are shown in Table 1. The
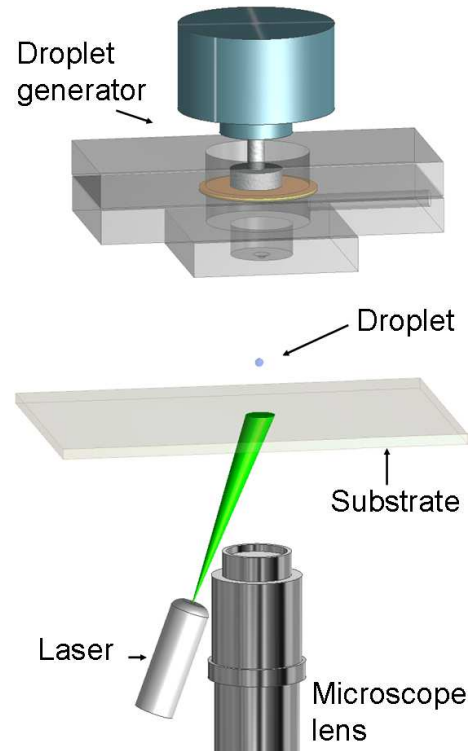

FIG. 1: (Colour online) Schematic view of the experimental setup.

glycerine and water solution was mixed with titanium dioxide (TiO_2) particles of ~ 2 μm diameter for the PIV visualization.

Droplets were jetted onto a transparent perplex rectangular sheet of 5 mm thickness placed 65 mm away from the nozzle plane. The droplet impact region was illuminated by a continuous laser beam positioned behind the substrate at an angle of 27 degrees from the substrate normal, see Fig. 1. The substrate was mounted on a translation stage with a micrometer control to precisely adjust the separation between coalescing droplets.

Density:	1222.0 ± 2.0 kg/m^3
Viscosity:	100.0 ± 0.5 mPa.s
Surface tension:	64.0 ± 0.5 mN/m
Static Contact angle:	63.2 ± 0.2 degrees
Droplet Speed of impact:	1.1 ± 0.1 m/s
Droplet diameter (in flight):	2.38 ± 0.03 mm
Droplet separation:	2.95 ± 0.03 mm
Time between droplets deposition:	10.0 ± 0.5 s

Table 1. Fluid and droplet properties.

The PIV technique requires two successive images taken in a short time interval to determine the motion of particles in a flow. In conventional PIV, the illumination

and the frame separation are usually provided and controlled by a twin laser system and a specialized camera, [10]. The correct utilization of this technique depends on many different variables and, as a consequence, its application is mostly restricted to systems with symmetrical geometries and to media with matched refractive indexes. In addition, the measurement of the fluid speed is limited by the frame rate, the field of view and the size and resolution of the CCD sensor and the optical system used for visualization. The measurement volume of a conventional PIV is determined by the field of view of the camera system and the width of the laser beam illuminating the flow (usually a laser sheet). In this work, an imaging setup consisting of a high speed camera coupled to a microscope lens was used for the PIV image acquisition. As a result, the time between successive images for the PIV analysis was determined and controlled by the frame speed of the high speed camera. The dimensions of the measurement region of this setup are determined by the field of view and the depth of field of the imaging system and not by the characteristics of the laser beam. A Phantom V7.3 monochrome high speed camera operating at a frame separation of 333.0 μs and a exposure time of 331.0 μs (3,000 fps option) was used with a Navitar 12x Zoom microscope lens system for the image acquisition. The camera system was pointed upwards to focus on the region of droplet impact on the substrate surface. The microscope zoom lens was set to produce a field of view of 10 mm $\times$ 7.5 mm. Under these conditions, the depth of field produced by the optical system was <200 μm and a resolution of 80 pixels/mm was achieved.

The axial position of the camera was adjusted to place the focal region on the substrate plane. The droplet impact and coalescence were illuminated by a laser beam with a 10 mm diameter at the landing plane. A CW laser diode with a wavelength of 532 nm and a maximum power of 200 mW was expanded by a 16.5 cm focal length aspheric lens and utilized as the light source.

The angle of incidence and the position of the laser light were chosen to minimize reflections. The maximum amplitude region of the beam was centered at the edge of the sessile droplet opposite to the impact. The laser beam was delivered with an angle of incidence of 27 degrees. For these experiments, the laser was operated at its maximum power, the camera set to its maximum sensitivity and the frame speed and size chosen to be the fastest and largest possible to show a clear view of the coalescence process. Examples of the images acquired by the experimental setup are shown in Fig. 2.

A second visualization setup was utilized to observe the impact and coalescence of droplets from a side view perpendicular to the substrate plane. For this imaging, the high speed camera was used with a macro lens Tamron SP AF90 set to its maximum magnification and maximum aperture. For the illumination, a 20 $\times$ 20 cm acrylic optical diffuser was placed between the substrate and a 500 W generic halogen lamp. The camera was angled a few degree downwards to clearly show the baseline of the
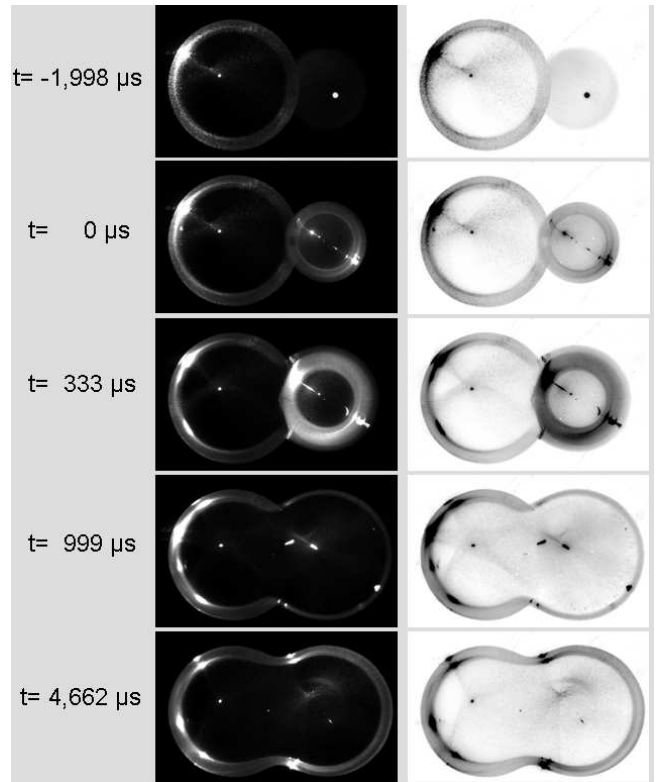

FIG. 2: (Colour online) Examples of images for drop impact and coalescence taken by the high speed image setup. The fluid used in these experiments was seeded with 2 μm TiO$_2$ particles to permit a PIV analysis. On the left, original images are shown. On the right, a digital negative is presented to facilitate the visualization of the contact line position.

droplets. Under these conditions, the high speed camera was operated at a frame separation of 149.0 μs and a exposure time of 2.0 μs. The resolution obtained by this setup is 40 pixels/mm, and examples of the recorded images are shown in Fig. 3.

B. Image analysis

The images experimentally obtained by the previously explained setup were digitally analyzed to obtain the geometrical properties of the coalescence process. Bottom-view images were analyzed to determine the composite droplet length, neck width and left and right droplet radii. Side view shadowgraph images were studied to establish the neck height and the contact angle. A diagram showing these properties is shown in Fig. 4. The Canny edge detection technique was used to find the drop outline for all the pictures in Matlab. For the bottom view, the maximum left and right point were then identified. The image was divided into two vertically down the center and the maximum and minimum vertical positions for each side were found. By combining these with the coordinates of the respective side position the intersect-
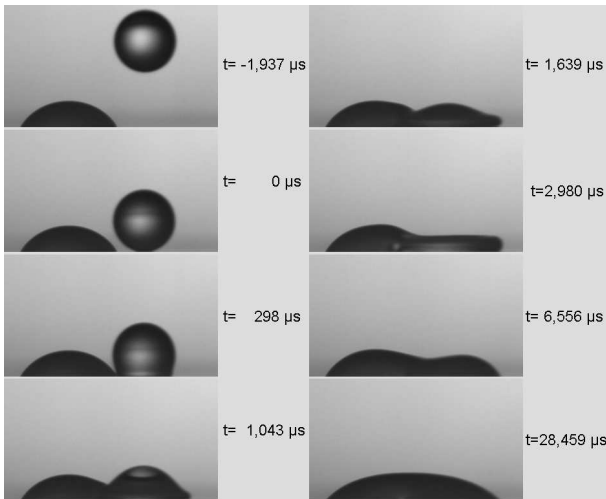
FIG. 3: (Colour online) Examples of images for drop impact and coalesce obtained by high speed shadowgraphy. In both, this series and the one shown in Fig. 2, the time = 0 μs corresponds to the frame showing the impacting droplet at the closest position from the substrate. As a consequence, a systematic timing error of up to 150 μs can exists between this side view and the bottom view shown in Fig. 2.
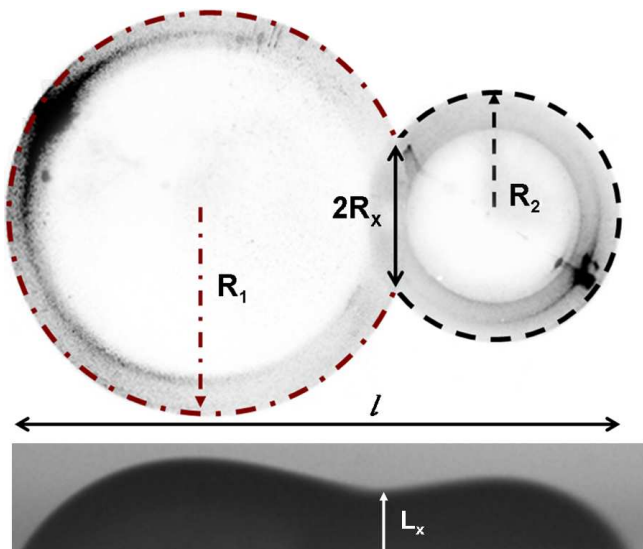

FIG. 4: (Colour online) Diagram of the quantities determined by the image processing.

ing chord theorem was used to estimate the radii of the left (R_1) and right (R_2) drop individually.

The neck width was found by splitting bottom-view images across the horizontal axis and analyzing the top and bottom section of the neck. The neck was found as the point closest to the central axis between the two maxima of the left and right drop peaks. From these coordinates the neck width and position from the left and right edge were found (R_x and l). In a similar way, side-view images were analyzed to obtain the neck height (L_z).

II. SIMULATIONS BY LATTICE BOLTZMANN METHOD

For comparison, the droplet coalescence process is here also analysed numerically using the lattice Boltzmann (LB) method [18]. This mesoscopic approach has the benefit that liquid free surfaces do not require special tracking or reconstruction at each time step; they arise naturally as part of the (liquid-gas) phase separation model, which in this case is the popular Shan-Chen multiphase model [19]. In addition, there is no need to specify the dynamic contact angle as an input to the model — only the equilibrium contact angle. These features make the method well suited to the simulation of flows involving both large and topological changes in free-surface shape, such as arise in droplet impact and coalescence. The LB method is also algorithmically much simpler than other diffuse-interface methods.

The 'lattice' in the LB method represents a discretisation of both 3D space and molecular velocity. Each node in the lattice has a set of vectors, $\vec{e}_a$ ($a = 0, \ldots, 18$), given by the displacements from the node to its 18 nearest neighbours plus the zero vector. The vectors $\vec{e}_a$ represent 19 molecular velocities, and each of these has associated with it a probability distribution function, f_a. The values of f_a across the whole lattice evolve in time according to a simple two-step process repeated at each time step: (i) the f_a at each lattice node relax towards a local Maxwellian distribution, and (ii) each f_a 'streams' along its associated vector to the neighbouring node. Thus step (i) represents molecular collision and step (ii) molecular motion.

Using a simple single relaxation time, τ, for all the f_a, the process can be written as

$$f_a(\vec{x} + \vec{e}_a, t + \Delta t) = f_a(\vec{x}, t) - \frac{[f_a(\vec{x}, t) - f_a^{eq}(\vec{x}, t)]}{\tau} \quad (1)$$

where the local Maxwellian equilibrium distribution is given by:

$$f_a^{eq}(\vec{x}, t) = w_a \rho \left[1 + 3\frac{\vec{e}_a \cdot \vec{u}}{c^2} + \frac{9}{2}\frac{(\vec{e}_a \cdot \vec{u})^2}{c^4} - \frac{3}{2}\frac{\vec{u}^2}{c^2} \right] \quad (2)$$

for $a = 0, \ldots, 18$. Here w_a are weights associated with each vector $\vec{e}_a$, $\vec{x}$ is the position within the lattice, t the time, Δt the time step, and c the lattice speed, while ρ and $\vec{u}$ are repectively the macroscopic density and velocity calculated as follows:

$$\rho(\vec{x}, t) = \sum_{a=0}^{18} f_a(\vec{x}, t) \quad (3)$$

$$\vec{u}(\vec{x}, t) = \sum_{a=0}^{18} \vec{e}_a f_a(\vec{x}, t) / \rho(\vec{x}, t) \quad (4)$$

For multiphase capability, the Shan-Chen model [19] introduces an interaction potential between neighboring

lattice nodes, which can be expressed as:

$$F(\vec{x}, t) = -G\psi(x, t) \sum_{a=0}^{18} w_a \psi(\vec{x} + \vec{e}_a, t)\vec{e}_a \qquad (5)$$

where F is fluid-fluid interaction force, G is an interaction strength parameter (negative for particle attraction), and ψ is a potential function that depends on density:

$$\psi(\rho) = \rho_0 \left[1 - \exp(-\rho/\rho_0)\right] \qquad (6)$$

where $\rho_0 = 1$. This model produces a non-ideal equation of state that supports the coexistence of a heavy phase of density ρ_h and a light phase of density ρ_l.

In order to simulate a droplet impacting onto a solid surface, a surface wetting model must also be introduced. Here this is achieved by specifying the fluid density on the solid surface via a 'surface affinity' parameter [20] defined in the range 0 to 1 by:

$$\eta = \frac{\rho_w - \rho_l}{\rho_h - \rho_l} \qquad (7)$$

where ρ_w is the density at the wall. Specifying η and using the calculated ρ_w results in an equilibrium contact angle between $0°$ ($\eta = 1$) and $180°$ ($\eta = 0$). In this study the choice $\eta = 0.4$ is used to give a static contact angle of $\theta_s = 63°$. This approach is sufficient to simulate the wettability of a perfectly smooth surface.
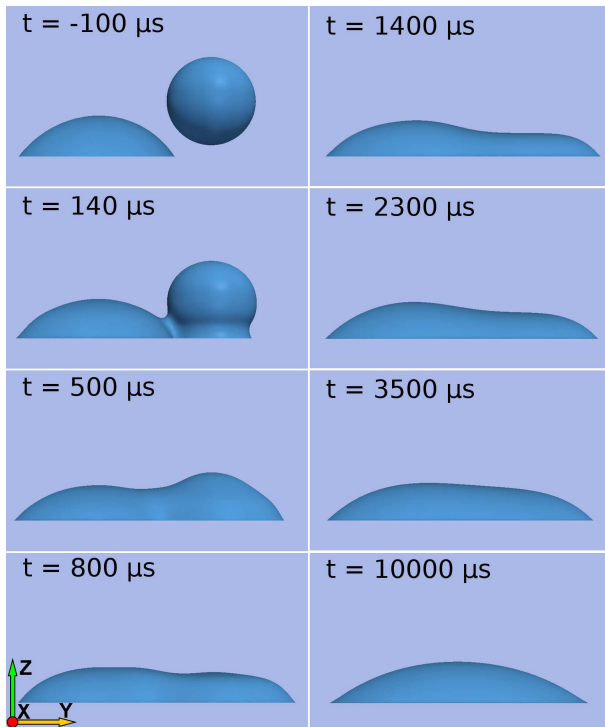

FIG. 5: (Colour online) Lattice Boltzmann simulation of droplet impact and coalescence corresponding to that in Fig. 3.

However, the properties of the surface can have a large influence on droplet deposition, spreading and coalescence. Owing to contact angle hysteresis, in the experiments (see below) only a small retraction of the contact line can be observed and the final footprint of the droplets after coalescence covers almost the same surface that was wetted during impact. For improved simulation of this phenomenon, a wetting model taking into account contact angle hysteresis and fluid adhesion on the solid surface is required. In this study, the model proposed in [21] is used. The surface affinity parameter (7) is initially set to correspond to the advancing contact angle $\theta_a = 85°$. Once the surface at a given location is wetted, i.e. when for the bottom wall:

$$\rho(x, y, z + 1) \geq \rho_l + H_a(\rho_h - \rho_l), \qquad (8)$$

the wettability properties change and the surface affinity at relevant nodes is changed to match the receding contact angle $\theta_r = 54°$, i.e. $\eta = f(\theta_r)$. Here $H_a = 0.9$ is a threshold parameter governing when the change will be applied. On the other hand, when the contact line starts to retract and the surface is dewetted, i.e. when

$$\rho(x, y, z + 1) \leq \rho_l + H_r(\rho_h - \rho_l), , \qquad (9)$$

the surface at the given location starts to recover its initial wettability properties back to θ_a over a time T_e, which corresponds to the physical time needed for evaporation of water molecules from the dewetted surface. Hence $\eta = f(\theta_a, T_e)$ in this case. The threshold parameter H_r ($= 0.1$) again controls the surface conditions under which this change is initiated. Such a wetting model gives more flexibility to define fluid-solid interactions and improve the ability to capture the effect of contact angle hysteresis in lattice Boltzmann simulations. Fig. 5 shows a visualisation of the lattice Boltzmann simulation corresponding to the experimental conditions in Fig. 3. Parameters used for LB simulation are as follows: $G = -4.5$, $\rho_h = 1.493$, $\rho_l = 0.253$, $\tau_h = 1.0$, $\tau_l = 0.9$, $gravity = 1.48 \cdot 10^{-6}$ and the initial droplet diameter was 40 lattice nodes.

III. RESULTS

A. Experimental

High speed bottom-view images were analyzed by two particle image velocimetry codes: URAPIV and MatPIV with similar results, [15, 16]. Consecutive high speed pictures were analyzed to detect the motion of the seeded particles to obtain internal velocity fields. As previously mentioned, the correct application of PIV analysis is conditioned to several variables including the particle displacement criterion. In these experiments, PIV analyses were only applied to image pairs showing a maximum particle displacement of less than 10 % of the size of the
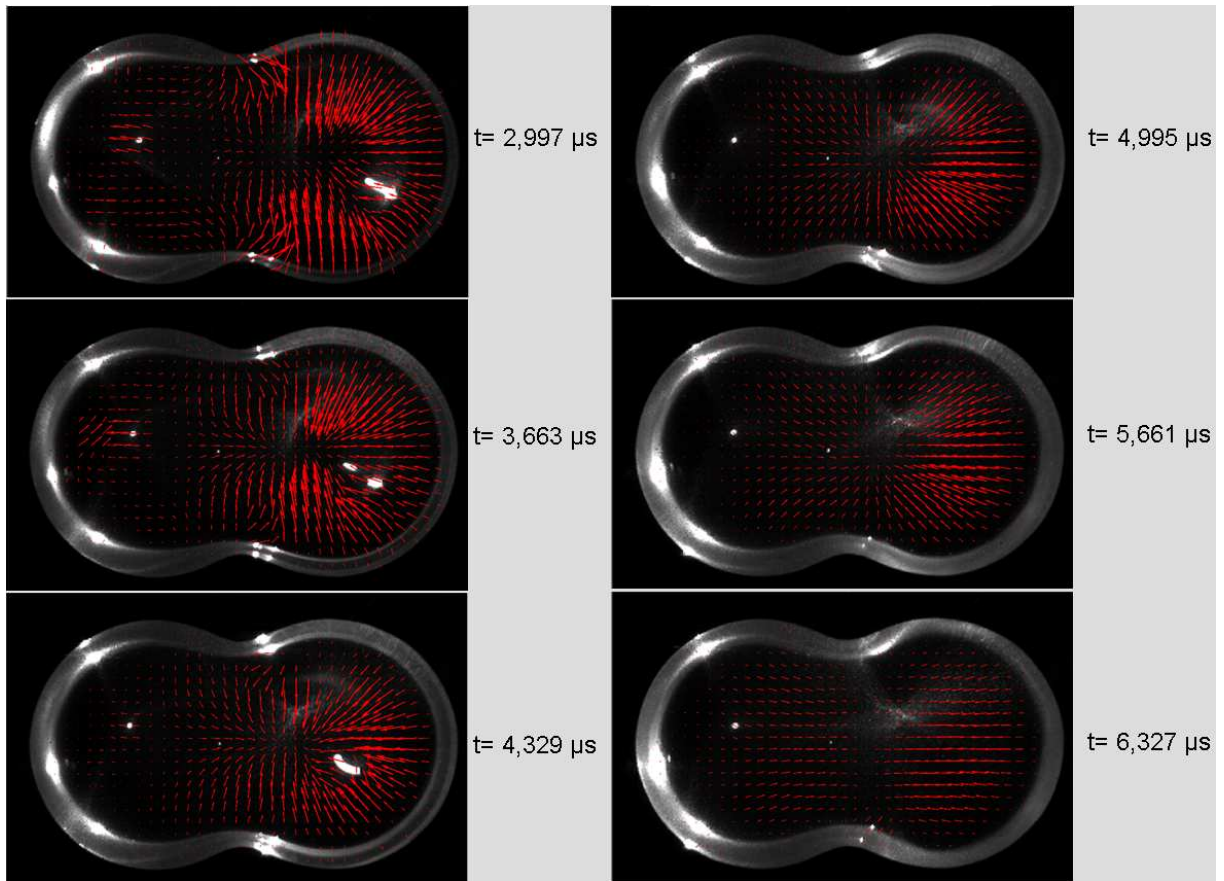
FIG. 6: (Colour online) Velocity fields on the coalescence of two glycerine and water droplets. The droplet on the right had impacted the substrate at a time = 0 μs, the droplet on the left was deposited 10 s earlier and is considered sessile. The velocity vectors around the laser reflections should not be considered as they produce spurious results.

interrogation area (64×64 pixels). As a result, appropriated PIV analyses were performed using consecutive images taken 3 ms after impact. This time corresponds to the region after maximum spreading, a phase usually described as the relaxation regime, [17]. Velocimetry studies at earlier times were restricted by the frame speed of the camera which was limited by the light conditions and its sensitivity. Experimental PIV results are shown in Fig. 6.

The velocity vectors surrounding the center of the recently deposited droplet suggest the existence of a convection-type circulation. This forced-convection flow is constantly shifted to the left until it is found at the center of the composite drop 6 ms after impact. It has been suggested that the mixing of coalescing droplets starts at the relaxation regime and these results agree with that thesis, [1].

For the experiments shown here the very early stages of coalescence differ from the case of two static drops merging. The second drop is impacting on the first such that it initially impacts the substrate, but as it spreads it merges into the first drop. For a single drop the spreading process is divided into the impact and wetting stages. The impact stage consists of the kinematic phase, spreading phase and relaxation phase. Therefore the initial stage of coalescence with an impacting drop can be divided into the same three phases. The side view images in Fig. 3 show the drop impact and spreading. The kinematic stage occurs for the first few hundred microseconds as the fluid in the second drop is moving vertically downwards. Beyond this, fluid begins to spread horizontally. This corresponds to the spreading phase of impact. This is when coalescence between the two drops starts. The fluid spreads outwards and the drop height of the second drop decreases forming a flattened disc shape corresponding to a maximum diameter, this occurs after approximately 3 ms. As the height of the second drop decreases below that of the first drop it can be assumed that the inertia causing the drop spreading is greater than the hydrostatic forces of the bulk fluid above. During the relaxation phase of spreading, or the intermediate stage of coalescence, the height of the second drop increases and the surface curvature decreases. After around 30 ms the drop reaches the final stage of coalescence and starts to relax into a spherical cap shape. The drop does not reach a spherical cap shape due to hysteresis of the contact angle causing pinning.

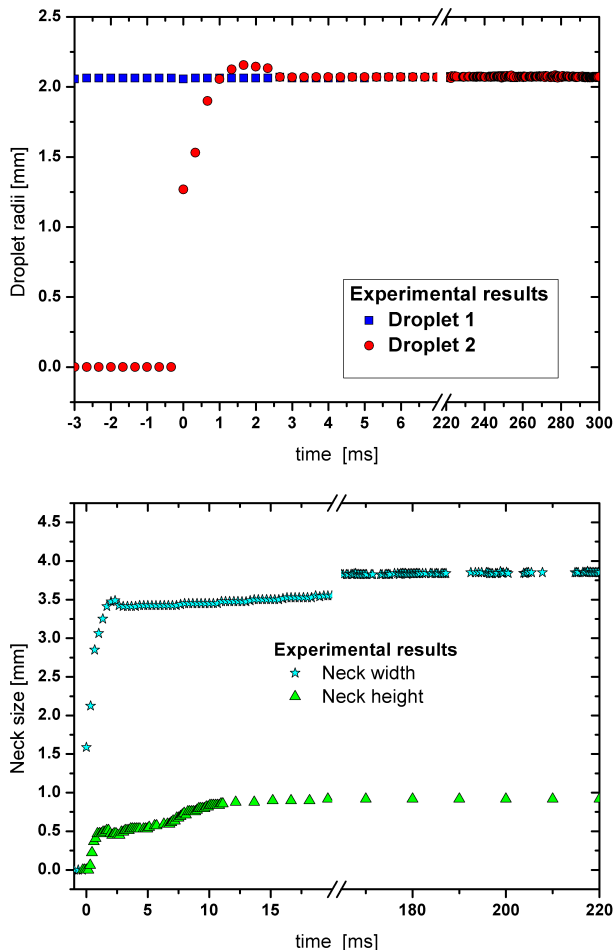The external dynamics of the impact and coalescence

FIG. 7: (Colour online) Temporal evolution of the measured droplet and neck features determined from the image processing

then begins to recover; its height increases, and a distinct neck once again forms, which grows much more slowly. From this point the development is similar to the static coalescence case.

B.   Computational

It has been observed before [22] that diffuse-interface models of wetting, such as the lattice Boltzmann method used here, have a tendency to overpredict the speed at which wetting occurs because, for computational efficiency, the liquid-gas interface thickness is generally larger than the true thickness. This effect is also seen in the simulations presented here, which show the coalescence process happening more quickly than in the experiments. However, it is interesting to check the qualitative behavior of the model against the experimental data.
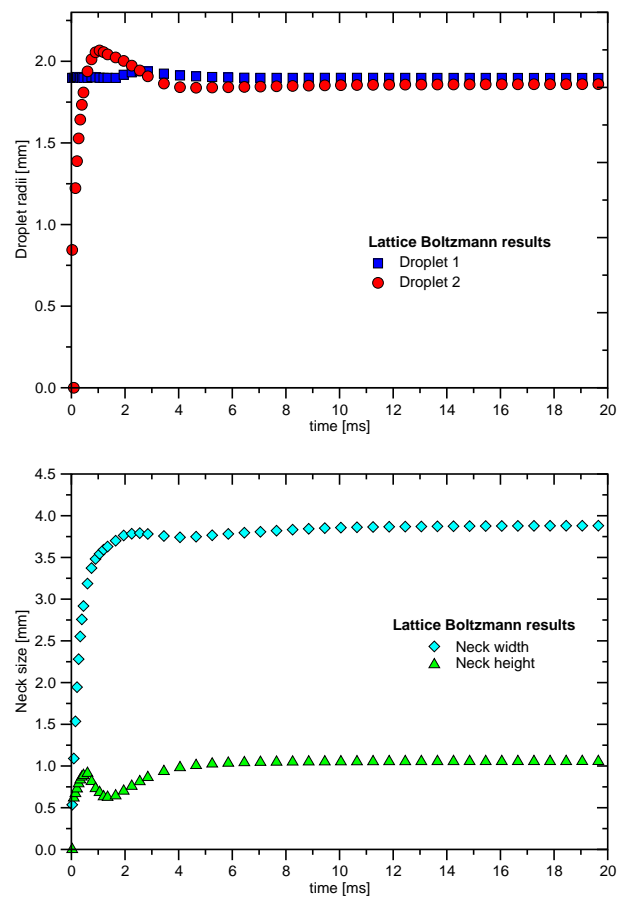

FIG. 8: (Colour online) Evolution of the droplet and neck features calculated from the lattice Boltzmann simulation.

process are quantified in Fig. 7, which shows the measured droplet radii (defined in Fig. 4), and the width and height of the growing 'neck' between them. The radius of the predeposited sessile droplet is remarkably unaffected by the impact of the second droplet. The radius of the impacting droplet grows very rapidly and expands beyond that of the sessile droplet as it spreads into its flattened disc, then it enters the retraction and much slower relaxation stage captured in the PIV results of Fig. 6.

The growth of the neck height is particularly telling when considering the differences between the impact-driven coalescence considered here and the capillary-driven coalescence of two static droplets. As the impacting droplet spreads, it quickly pushes into the sessile droplet and swiftly closes the gap between them. The neck height therefore increases very rapidly in this stage, until it becomes commensurate with the height of the disc formed when the second droplet is at its maximum extent. At this stage it is difficult to define a clear 'neck' in the side views (Figs. 3 and 5), and the neck height profile shows a plateau corresponding to the height of the flattened second droplet. However, the flattened droplet

The simulation predictions of the droplet radii and neck growth are given in Fig. 8. Despite overpredicting the rate at which the changes occur, the simulation captures well the essential features such as the spreading of the second droplet to its maximum extent, and subsequent recoil. The growth of the neck height again shows the different behaviour at different stages: the very rapid
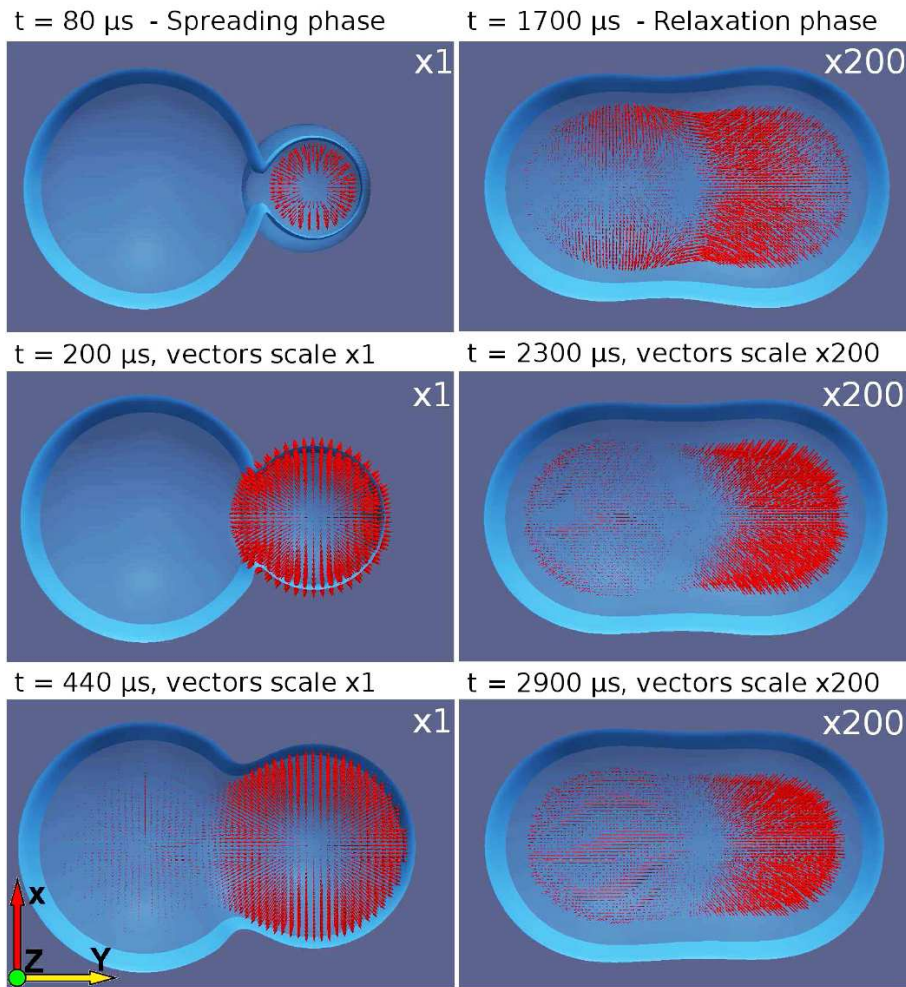
FIG. 9: (Colour online) Velocity fields calculated from the Lattice Boltzmann simulation of the coalescence of two droplets. The droplet on the right had impacted the substrate at a time $= 0$ μs, the droplet on the left was deposited in previous simulation and is considered sessile. Note that the velocity vectors in the right-hand images are magnified 200 times compared to those on the left.

initial increase in height as the gap between the droplets is closed, and the later, slower relaxation. However, the simulation overpredicts the extent to which the second droplet merges with the first in the initial impact stage (as can be seen by comparing Fig. 5 with Fig. 3). Hence there is actually a reduction in neck height as the second droplet flattens. Again, the 'neck' is not distinct at this stage. Another cause for a slight discrepancy between the simulation and experiment is that in the simulation the neck height is calculated based on the local minimum in the free surface height measured along the centreline. Hence any concavity on the surface would produce a lower value of the neck since in the experimental side view, one cannot see past the higher outer part of the droplet.

Fig. 9 shows the droplet impact simulation viewed from below the substrate, mimicking the arrangement of the experimental PIV system, and showing the calculated velocity vectors. The images in the left-hand column of the figure show the spreading stage of the droplet deposition, while those on the right show the retraction. Focusing on the right-hand column, these show good agreement with the generic features of the experimental PIV results of Fig. 6: the flow is focused towards a point on the centreline between the neck and the centre of the second droplet. As in the experiments, the flow is mainly from the right, consistent with the recoil of the droplet seen in Fig. 3. The footprint of the combined drop does not show as pronounced a peanut shape as in the experiments, but with the inclusion of contact angle hysteresis in the model it does retain an elongated shape rather than relaxing to a circular footprint.

To give an indication of the speed of flow in the earlier stages of the impact and coalescence, the left-hand column of Fig. 9 shows the expansion stage of the impacting drop. It is important to note the difference in scale of the velocity vectors in the two columns — the vectors in the right-hand images are magnified by a factor of 200 compared to those on the left. Hence the velocities in the initial stage are two orders of magnitude higher than

those captured in the PIV analysis, highlighting the challenge in visualizing the internal dynamics of the droplets in the earlier stages. The simulation results also indicate that the pre-deposited droplet is essentially inert in the initial coalescence stage.

IV. CONCLUSIONS

An experimental configuration that allows the visualization of the internal dynamics and surface motion of drops impacting and coalescing onto a transparent substrate has been presented. Particle image velocimetry has been used to obtain the internal velocity field of coalescing droplets and these results compared with numerical simulations. The velocity fields obtained reveal that during the recoil of the impacting droplet, a flow is induced from the otherwise inert pre-deposited droplet towards the second droplet. This supports the suggestion that mixing between droplets begins at the relaxation stage of coalescence.

Side-view shadowgraph pictures of the same experiment were analyzed to determine the geometrical characteristics of the coalescence process. The growth of the neck height in particular highlights the difference between this impact-driven coalescence and the coalescence of two static droplets. The neck height initially increases more rapidly in the impact-driven case, as the gap between the droplets is closed by the rapid spreading of the second droplet. The neck then becomes difficult to distinguish from the side view, and the height levels off at the height of the fully spread second droplet, before becoming more distinct again as the second droplet regains its height and coalescence proceeds as in the static droplet case. The lattice Boltzmann simulations slightly overpredict the speed at which coalescence takes place, but capture the main features of the process.

The comparison of experimental and computational results presented here highlights two important points. Firstly, the quantitative differences between the experimental and numerical data demonstrate the need for good experimental visualization and quantification of flows, both internally and externally, in order to validate computational methods. Secondly, the numerical predictions of the fluid velocities in the early stages illustrate the challenges in developing experimental systems capable of analysing the internal dynamics of droplets in the early stages of impact and coalescence.

[1] M. Sellier and E. Trelluyer, *Biomicrofluidics*, **3** 022412 (2009).

[2] R.E. Saunders, J.E. Gougha and B. Derby, *Biomaterials*, **29** 193 (2008).

[3] M. Kaneda, *et.al.*, *Langmuir*, **24** 9102 (2008).

[4] N. Kapur and P.H. Gaskell, *Phys. Rev. E*, **75** 056315 (2007).

[5] A. Menchaca-Rocha, A. Martínez-Dávalos, R. Núñez, S. Popinet, S. Zaleski, *Phys. Rev. E*, **63** 046309 (2001).

[6] J. Eggers, J.R. Lister, H.A. Stone, *J. Fluid Mech.*, **401** pp. 293-310 (1999).

[7] L. Duchemin, J. Eggers, C. Josserand, *J. Fluid Mech.*, **487** pp. 167-178 (2003).

[8] W.D. Ristenpart, P.M. McCalla, P.V. Roy, H.A. Stone, *Phys. Rev. Lett.*, **97** 064501 (2006).

[9] K.H. Kang, S.J. Lee, C.M. Lee and I.S. Kang, *Meas. Sci. Technol.*, **15** 1104 (2004).

[10] C. Ortiz-Dueñas, J. Kim and E.K. Longmire, *Exp. Fluids*, **49** 111 (2010).

[11] J. Kim and and E.K. Longmire, *Exp. Fluids*, **47** 263 (2009).

[12] G.S. Settles, *Schlieren and Shadowgraph Techniques: Visualizing Phenomena in Transparent Media*, (Springer, Heidelberg 2001).

[13] A. Frohn and N. Roth, *Dynamics of Droplets*, (Springer Verlag, Berlin 2000).

[14] J.R. Castrejón-Pita, G. Martin, S. Hoath and I. Hutchings, *Rev. Sci. Instrm.*, **79** 075108 (2008).

[15] Z. Taylor, R. Gurka, A. Liberzon and G. Kropp, *Proceedings of the 61st Annual Meeting of the Division of Fluid Dynamics of the American Physical Society, San Antonio, Texas, November 23-25* (2008).

[16] J. K. Sveen, *An Introduction to MatPIV v.1.6.1*, (Department of Mathematics, University of Oslo, ISSN 0809-4403, 2004).

[17] W.K. Hsiao, S.D. Hoath, G.D. Martin and I.M. Hutchings *Journal of Imaging Science and Technology*, **35** 050304 (2009).

[18] S. Succi, *The Lattice Boltzmann Equation for Fluid Dynamics and Beyond*, Oxford University Press (2001).

[19] X. Shan and H. Chen, *Phys. Rev. E*, **47** 1815–1819 (1993).

[20] D. Iwahara, H. Shinto, M. Miyahara and K. Higashitani, *Langmuir*, **19**(21), 90869093 (2003).

[21] K.J. Kubiak, M.C.T. Wilson, J.L. Summers, N. Kapur, K. Hood, *Proceedings of the 63st Annual Meeting of the Division of Fluid Dynamics of the American Physical Society, Long Beach, California, November 21-23* (2010).

[22] J.M. Yeomans, *Physica A*, **369**, 159-184 (2006).